Electronic Supplementary Material (ESI) for Environmental Science: Nano.

SUPPLEMENTARY DATA

Long-Term Effects of TBBPA-Contaminated Pyrogenic Organic Matters under The Abiotic Aging: Insights on Immobilization Capacity, Surface Functionality Correlation, and Phytotoxicity to *Thinopyrum ponticum*

Jian Shen[a], *Guohe Huang*[a,*], *Chunjiang An*[b], *Yao Yao*[a], *Peng Zhang*[a] *Xiaying Xin*[a], *Scott Rosendahl*[c]

[a] Institute for Energy, Environment and Sustainable Communities, University of Regina, Regina, Saskatchewan, Canada S4S 0A2

[b] Department of Building, Civil and Environmental Engineering, Concordia University, Montreal, Quebec, H3G 1M8, Canada

[c] Canadian Light Source, Saskatoon, Canada S7N 2V3

MATERIALS AND METHODS

2.1 Chemicals

TBBPA (4,40-isopropylidenebis(2,6-dibromophenol)) with a purity greater than 97% was purchased from Aldrich Chemical Co. (WI, USA). Methanol (HPLC grade) was obtained from VWR Scientific (AB, Canada). The standard solution was prepared by dissolving TBBPA into methanol for a concentration of 200 mg/L. All other chemicals used were of reagent-grade quality or higher. High-purity water was used in all experiments, prepared by processing deionized water through a Milli-Q system.

2.2 Collecting, Preparation, and Aging of Pyrogenic Organic Matter

The manner of the POM production was informed by the consideration that POM can be produced through both natural generation and manufacture. Given that they are widely distributed in cold regions and recognized as an agricultural waste in field and gardening, pinecone species were used in this study. The pinecone biomass was collected from Yellow pines (*Pinus. ponderosa*) from southern Saskatchewan, Canada. The procedure of preparing the natural charcoal was in accordance with the standard method described by Peng et al. (2016). The pinecones were separated and washed with deionized water to remove impurities, and then air-dried for 2 days before being oven-dried at 110 °C for 24 hr. After drying, the biomass samples were grounded and passed through a 0.425 mm standard sieve. The resultant fine pinecone powder was tightly packed into a ceramic pot and covered with aluminum foil, then

pyrolyzed for 4 hr at high (550 °C) and low (250 °C) temperatures in a muffle furnace (within an oxygen-limited system). The heating rate was maintained at 5 °C/min. The pyrolyzed carbon was then centrifuged to remove supernatants and washed with pure water to achieve a neutral pH. The samples were further oven-dried for 24 hr at 85 °C. (The POM specimens were labeled as "NCs"). To represent wildfire-generated natural charcoal, low temperatures (250 °C) and high temperatures (550 °C) were applied in the pyrolysis process to produce POM specimens, referred to as NC250 and NC550, respectively. To simulate the impacts of abiotic aging, the aged POM was produced by subjecting the specimens to repeated freeze-thaw cycles[1]. The freeze-thaw treatment was performed in a total of 21 freeze-thaw iterations comprising cold conditions (−20 °C) for 7 hr and warm conditions (30 °C) for 17 hr. The POM specimens aged through abiotic aging are referred to herein as LPNC250 and LPNC550.

2.3 TBBPA Immobilization Studies on Pyrogenic Organic Matter

The immobilization aspects of POM, including specific TBBPA transport behaviors, were investigated via several batch adsorption experiments (Figure.S1). Batch adsorption experiments were carried out in 20 mL volumetric glass vials capped with aluminum foil. Appropriate amounts of pyrolyzed carbon (10 mg) and TBBPA at specific concentrations were added to each vial. Preliminary experiments showed that 24 hours would be sufficient for the adsorption process to reach equilibrium. To investigate the specific surface effects on POM and study the changes in surface aging, 10 mg of NCs and LPNCs were added into each glass vial with a defined initial TBBPA concentration. To investigate the transport of TBBPA species under pH conditions, amounts of 0.01 M NaOH and HCl were added into each glass vial with initial

TBBPA concentrations ranging from 0.5 mg/L to 2 mg/L. Sorption experiments for TBBPA were conducted for all application rates of pyrolyzed carbon. In the kinetics experiments, TBBPA concentrations were monitored at time intervals under temperatures of 15 °C, 25 °C, and 35 °C. The behavior of the DOM during TBBPA adsorption on the pyrolyzed carbon surface was analyzed by adding different concentrations of humic acid sodium salt (ranging from 10 mg/L to 30 mg/L) before adding the TBBPA.

The TBBPA stock solution was prepared in methanol and then diluted using background solutions of 0.01 M $CaCl_2$ and 200 mg/L NaN_3 to simulate constant ionic strength in environmental water and to inhibit microbial activity, respectively. It should be noted that methanol concentrations (methanol/water, v/v) were controlled at less than 0.1% to avoid co-solvent effects. Initial concentrations (0.5 mg/L to 2.0 mg/L) were determined that would cover the range from detection limit to aqueous solubility. Blank controls (i.e., without sorbents) were run concurrently to investigate sorption to the walls of the glassware. It should also be noted that the experiments were conducted in the dark to prevent photolysis.

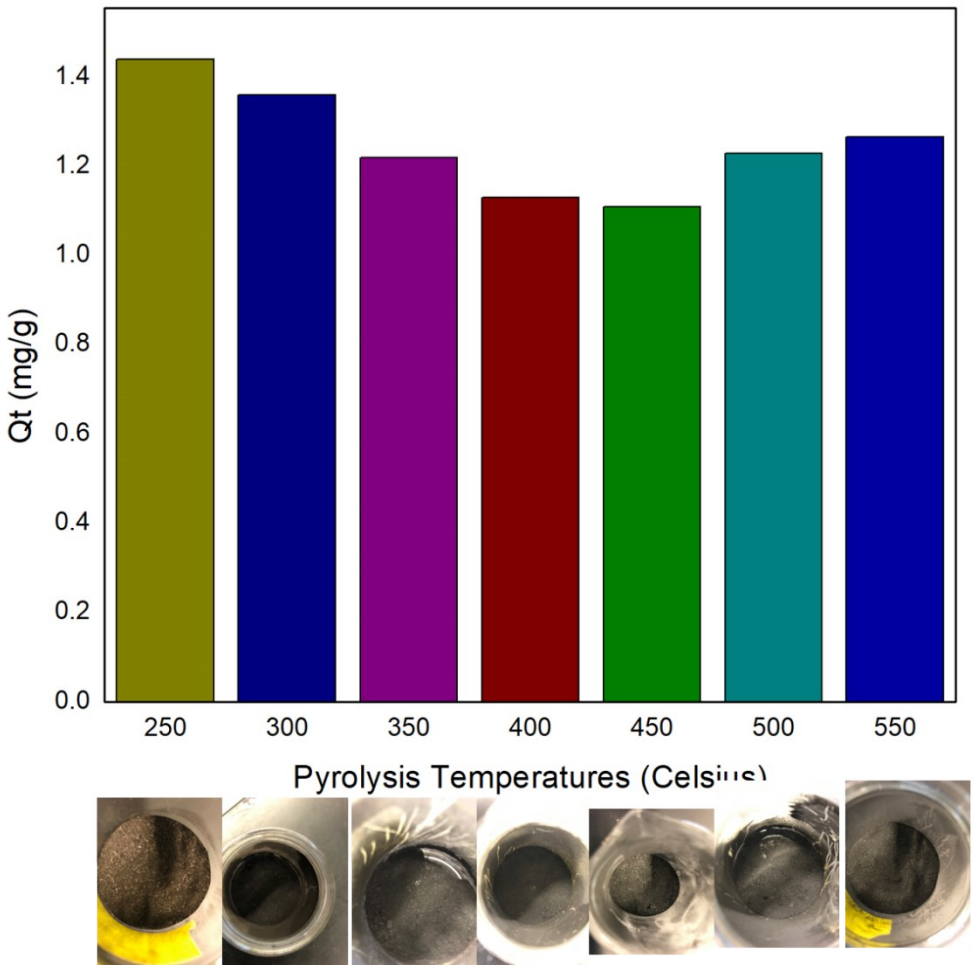

Figure.S1 Produced POMs with pyrolysis temperatures from 250 ~ 550 ℃, and corresponding adsorption rates

2.4 Analytical methods

Under the influence of DOM, the surface interaction between POM and TBBPA was analyzed using the synchrotron FTIR analysis method. Given that high-brilliance synchrotron radiation can help to ensure results with adequate signal-to-noise ratio, even with small apertures[2],

synchrotron FTIR analysis was carried out at the 01B1-01 (MidIR) beamline of the Canadian Light Source facility (Saskatoon, Canada). A Bruker Vertex 70v interferometer with a liquid nitrogen-cooled mercury cadmium telluride (MCT) detector was applied in order to analyze the samples using synchrotron infrared (IR) light. To compensate for changes in atmospheric conditions and synchrotron ring current, background spectrum was taken for each sample. A focal plane array (FPA) imaging mode was used to collect IR images of pyrolyzed carbon surface[3]. The spectral range from 900 cm^{-1} to 3,400 cm^{-1} was collected at 4 cm^{-1} resolution. Spectra were measured with 512 co-added scans, with the data collected and analyzed using OPUS 7.2 software (Bruker, USA). Raw spectra were processed using 12-point smoothing and baseline correction.

An Agilent Infinity 1260 high-performance liquid chromatography system (USA) equipped with a ZORBAX XDB-C18 column and a diode array detector (DAD) operated at a wavelength of 210 nm was used to measure the concentration of TBBPA. A mobile phase consisting of methanol/water (85:15, v/v) was used at a flow rate of 0.7 mL/min. SEM images were collected for the selected samples (BCYP300, BCYP 600, BCBP300 and BCBP 600) using a Zeiss Supra 55 VP SEM (Germany) with an accelerating voltage of 5.00 kV. The specific surface area of pyrolyzed carbon was determined at 77 K using a TriStar II 3020 (Micromeritics, USA).

Use of an atomic force microscope (AFM), it should be noted, is a versatile technique for studying the surface of particles such as POM at a nano scale. [4] In our study, this was carried out using an atomic force microscope (Bruker Innova, Germany) to analyze the topography (3D view) of the POM particles. The 3D arrangement of the topography, meanwhile, served to

capture the physical attributes (such as height, shape, and depth) of a surface in a given region. [5]

2.5 QA/QC

The adsorption capacity of Q_t and the percentage removal were calculated using Equation (1) and Equation (2), respectively.

$$Q_t = \frac{(C_i - C_e)V/1000}{W} \quad (1)$$

$$\%\, removal = \frac{C_i - C_e}{C_i} \times 100 \quad (2)$$

where Q_t is the adsorption capacity in mg g^{-1} at time *t*, C_i and C_e are the initial and equilibrium concentration (mg L^{-1}), V is the volume of the solution (mL), and W is the total mass of adsorbent (g).

In the TBBPA adsorption experiment, the adsorption capacity of the pyrolyzed carbon at equilibrium was calculated using the following equation:

$$q_e = \frac{V(C_0 - C_e)}{m} \quad (3)$$

where q_e is the amount of TBBPA adsorbed at equilibrium time (mg kg^{-1}); C_0 and C_e (mg L−1)

are the initial and equilibrium concentrations of TBBPA in the solution phase, respectively; V is the solution volume (L); and m is the mass of dry pyrolyzed carbon (g).

A quality assurance program was followed to ensure the accuracy and reliability of the collected data. All batch experiments were conducted in triplicate, and the average values were recorded (relative standard deviation less than 5%). Blank tests were run and corrections were applied if necessary. All containers used in this study had been previously cleaned with a cleaning solution formulated specifically for laboratory experiment purposes, triply rinsed with distilled water, and oven dried. Experimental runs were performed using a TBBPA solution containing no pyrolyzed carbon. The corresponding results confirmed that the initial TBBPA concentration remained unchanged during the experiment, in turn indicating that any reduction in TBBPA concentration observed in the experiments was the result of adsorption on the pyrolyzed carbon samples.

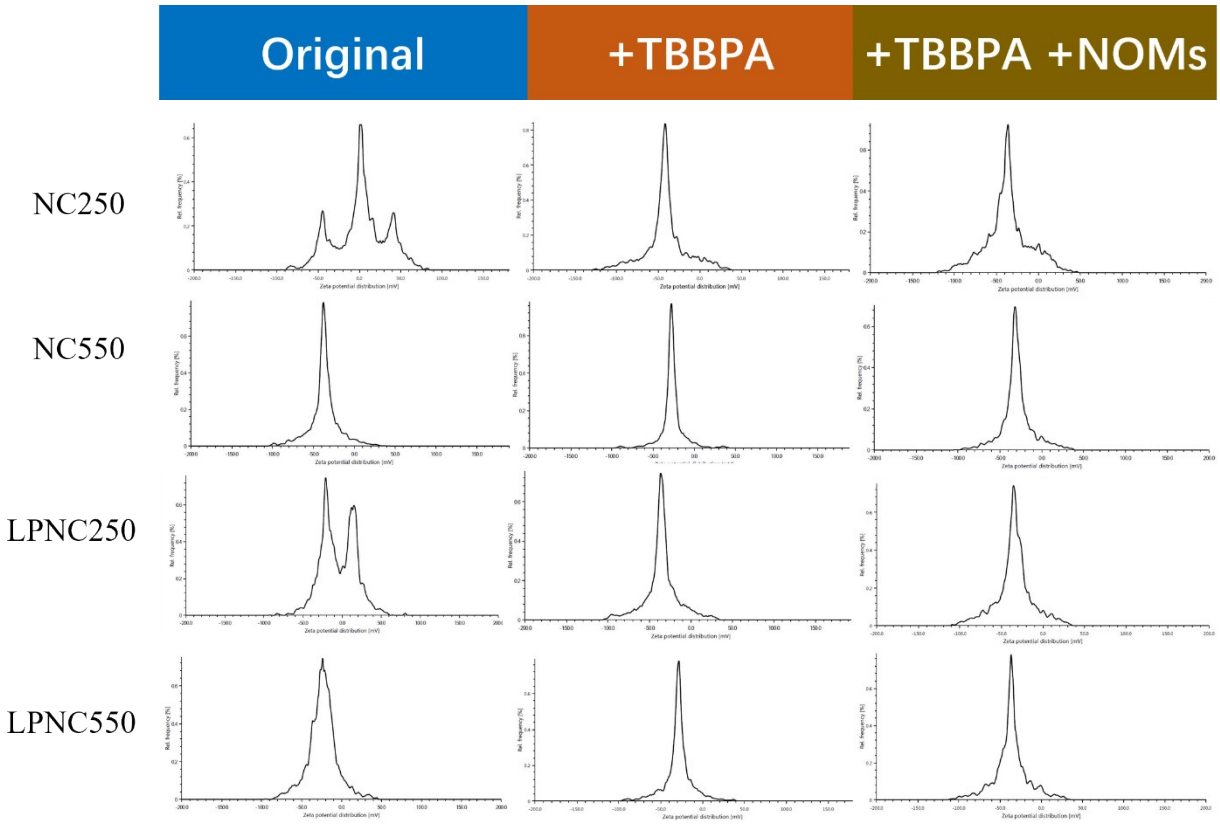

Figure.S2. Zeta-potential results for POMs and the response after the adding of TBBPA and NOMs

RESULTS AND DISCUSSION

S3.1 Adsorption isotherms analysis in different temperatures

The equilibrium retention of TBBPA onto pyrogenic carbon with different surface properties can be mathematically described via numerical models with physical-chemical assumption and empirical inference. Types of surface coverage including homogeneity and heterogeneity were considered in those models. The surface interactions between TBBPA and function groups were further explored using adsorption isotherm modeling. Langmuir, Freundlich and Langmuir-

Freundlich isotherm models were used in this study(Supporting Information).[6] The adsorption isotherms and calculated results are shown in Figure. S3, Table S1 and Table. S2, respectively. The Langmuir isotherm can be expressed as follow:

$$Q_e = \frac{q_m K_L C_e}{1 + K_L C_e} \quad (4)$$

where q_e (mg/g) and C_e (mg/L) are the amount of sorbed TBBPA per unit mass of adsorbent and TBBPA concentration at equilibrium, respectively. q_m (mg/g) is the maximum amount of the TBBPA per unit mass of adsorbent to form a complete monolayer on the surface. K_L is a constant related to the affinity of the binding sites (L/mg).

The Freundlich isotherm model, an empirical equation, is used to describe heterogeneous surfaces [7]. The Freundlich equation is:

$$Q_e = K_F C_e^{\frac{1}{n}} \quad (5)$$

where K_F is an empirical constant related to the sorption capacity of the adsorbent (L mg^{-1}) and constant n is an empirical parameter related to the intensity of sorption and varies with surface heterogeneity and affinity. The value of n gives an indication of the favorability of the sorption.

The Langmuir-Freundlich isotherm model [8] is:

$$Q_e = \frac{q_{m^*} b C_e^{n^*}}{1 + b C_e^{n^*}} \quad (6)$$

b is the adsorption equilibrium constant relating to the binding energy of the adsorption system. n^* is indicative of the surface site heterogeneity of the adsorbent.

Figure. S3 shows the adsorption patterns on varied carbon surfaces are different. When the environmental temperature increased from 288 K to 308 K, the uptake of TBBPA generally decreased. It indicates the adsorption is an exothermic process for various pyrolysis and physical aging conditions. Such exothermic feature for TBBPA adsorption was also found on other carbon materials such as graphene oxide[9] and carbon nanotube.[7] Additionally, the involvement of NOMs can have significant impact on adsorption under different environmental temperatures. That suggests NOMs can result in unneglectable thermodynamic changes in the interaction between TBBPA and carbon surfaces. With the increased amount of NOMs, the uptake of TBBPA on carbon surfaces is decreased and the interaction is changed to the endothermic process.

When Freundlich model presents good fitting, it indicates a multilayer adsorption is involved between adsorbed TBBPA and carbon surfaces.[10] The n values higher than 1 suggest the adsorption is favorable and the active sites on the carbon surface for TBBPA are heterogeneous for TBBPA adsorption. Nevertheless, as the relatively high R^2 of Langmuir model is approached, the adsorption can be more suitable to be described as the formation of monolayer coverage on the carbon surface. When the R_L value is below than 1, the adsorption of TBBPA on carbon

surface could be favorable. Q_m significantly decreases with the involvement of NOMs, suggesting NOMs can cause great negative impact on TBBPA adsorption. Moreover, the Langmuir-Freundlich isotherm model showed a better overall fitting than Langmuir and Freundlich isotherm models. It indicates both heterogenetic and monolayer adsorption can be involved. The deviation of n^* value from 1 shows that the multilayer adsorption could take place for attracting TBBPA to the active sites on heterogenous surface.

n values from Freundlich isotherm model for BCP250 and BCP550 in non-NOMs solution increase for FTBCP250 and FTBCP550 after physical aging. It indicates that the physical aging process can result in more active sites on the extended heterogenous carbon surfaces for TBBPA adsorption. However, n^* from Langmuir-Freundlich model drops down after physical aging process. It can be attributed to the increasing surface area and surface complexity, which enhances physical adsorption on porous surface rather than attraction to the active sites. Additionally, after adding NOMs, an increase in n value is observed on most carbon surfaces. It can be explained that the involvement of NOMs can enhance the multilayer adsorption because NOMs could capture and replace the active sites on the heterogenous surface and compete with TBBPA. The n^* values slightly increase after adding NOMs. It suggests that physical adsorption can be reduced due to the decrease of surface tension. As most pores are filled with NOMs, the active sites struggle to attract TBBPA to the carbon surface from NOMs solution.

S3.2 Thermodynamic analysis of NOMs competing adsorption

The changes in thermal performances and thermodynamic characteristics of adsorption reflects

the impacts of NOMs solutions (Table S3 and S4). The adsorption of TBBPA on carbon surface competed with NOMs in the solution, resulting the highest TBBPA adsorption at 298 K compared to the adsorption at 288 and 303 K in the presence of 10 mg/L of NOMs. It can be explained that during the competition with NOMs, the system also had some endothermic NOMs-TBBPA interactions, such as solubilization and surface activity effects. The endothermic reactions can thus compete with exothermic reactions at different temperatures, resulting in inconsistent thermodynamic behavior of TBBPA on carbon surface. Additionally, in both 10 and 30 mg/L NOMs solutions, ΔS° exhibited positive values, indicating TBBPA in the system was partially dispersed. The positive ΔH° values showed that external energy was needed for TBBPA uptake and partial TBBPA might need external energies to be subtracted from NOMs solutions. Moreover, the calculated thermodynamic parameters based on K_c and K_F indicated that, as the ΔG° showed negative value, the adsorption was still carried out spontaneously, even the thermal performance switched from exothermic to endothermic reactions.

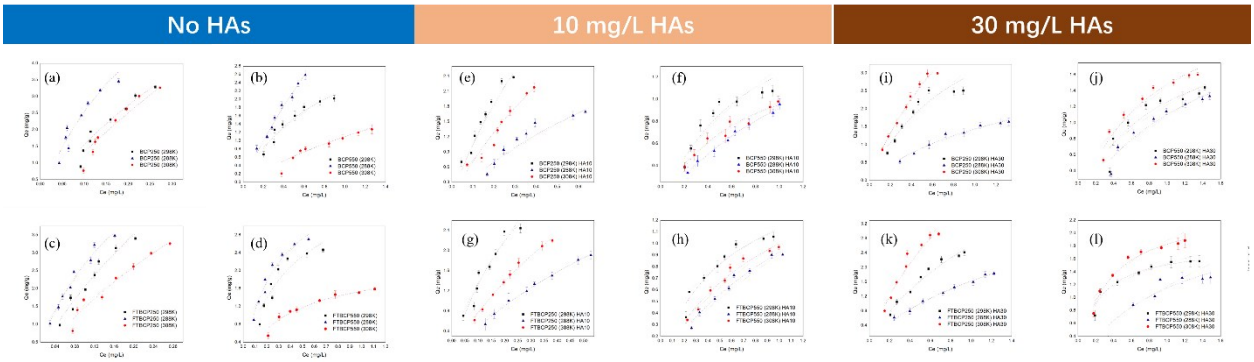

Figure.S3. Fitted adsorption data with Langmuir model (purple dash line) and Freundlich model (yellow dot line) for (a) BCP250, (b) BCP550, (c) FTBCP250, and (d) FTBCP550 in water, (e)

BCP250, (f) BCP550, (g) FTBCP250, and (h) FTBCP550 in 10 mg/L HAs, (i) BCP250, (j) BCP550, (k) FTBCP250, and (l) FTBCP550 in 30 mg/L HAs.

Table S1. Calculated parameters of isotherm models for TBBPA adsorption under different NOMs solution

Humic Acid	Adsorbent	Temperature (K)	Langmuir				Freundlich		
			Q_m (mg/g)	K_L (L/mg)	R_L	R^2	1/n	K_F (mg/g)	R^2
No HAs	BCP250	288	9.350	3.740	0.118	0.947	1.337	14.020	0.930
		298	11.201	1.616	0.236	0.858	1.253	9.824	0.849
		308	21.576	0.658	0.432	0.963	1.112	10.562	0.960
	BCP550	288	11.634	0.470	0.515	0.975	1.176	3.986	0.975
		298	3.960	1.276	0.282	0.939	1.600	2.313	0.909
		308	4.436	0.330	0.602	0.859	1.232	1.100	0.847
	FTBCP250	288	7.637	5.462	0.084	0.974	1.466	12.701	0.960
		298	11.810	2.106	0.192	0.980	1.241	12.982	0.943
		308	11.899	1.405	0.262	0.948	1.333	8.754	0.955
	FTBCP550	288	4.263	3.519	0.124	0.960	1.957	3.910	0.920
		298	4.174	2.516	0.166	0.865	1.828	3.310	0.814
		308	2.228	2.259	0.181	0.959	2.336	1.549	0.916
10 mg/L HAs	BCP250	288	5.305	0.765	0.395	0.938	1.250	2.519	0.923
		298	8.284	1.441	0.258	0.963	1.236	6.710	0.953
		308	7.450	1.047	0.323	0.952	1.261	4.589	0.964
	BCP550	288	2.026	0.826	0.377	0.986	1.513	0.927	0.988
		298	2.073	1.432	0.259	0.895	1.618	1.286	0.837
		308	1.503	1.720	0.225	0.964	1.898	0.973	0.952
	FTBCP250	288	6.338	0.827	0.377	0.994	1.300	3.189	0.986
		298	6.039	2.821	0.151	0.928	1.445	6.701	0.884
		308	7.161	1.199	0.294	0.992	1.259	4.899	0.984
	FTBCP550	288	2.583	0.557	0.473	0.970	1.263	0.909	0.967
		298	1.743	1.792	0.218	0.930	2.123	1.139	0.908
		308	2.041	0.959	0.343	0.968	1.431	1.009	0.976
30 mg/L HAs	BCP250	288	3.510	0.697	0.418	0.971	1.504	1.423	0.952
		298	5.647	1.138	0.305	0.912	1.466	3.211	0.864
		308	8.277	0.968	0.341	0.977	1.297	4.563	0.982
	BCP550	288	2.699	0.692	0.419	0.926	1.555	1.801	0.898
		298	2.331	1.177	0.298	0.844	1.838	1.222	0.787
		308	2.724	1.185	0.297	0.930	1.923	1.447	0.904
	FTBCP250	288	4.272	0.614	0.449	0.993	1.445	1.615	0.992
		298	6.178	0.719	0.410	0.967	1.408	2.649	0.953
		308	8.271	0.853	0.370	0.970	1.350	4.176	0.928
	FTBCP550	288	2.389	0.930	0.350	0.889	1.527	1.176	0.833
		298	1.818	4.922	0.092	0.932	3.571	1.529	0.880
		308	2.394	3.245	0.134	0.973	2.688	1.886	0.911

Table S2. Thermodynamic parameters calculated from different K values

DOMs	Carbon surface	Kc based				KL based				KF based			
		T (K)	ΔG (kJ/mol)	ΔH (kJ/mol)	ΔS (kJ/mol)	T (K)	ΔG (kJ/mol)	ΔH (kJ/mol)	ΔS (kJ/mol)	T (K)	ΔG (kJ/mol)	ΔH (kJ/mol)	ΔS (kJ/mol)
No HAs	BCP250	288	-7.532	-24.568	-0.058	288	-3.158	-64.018	-0.211	288	-6.322	-10.616	-0.015
		298	-7.012			298	-1.189			298	-5.661		
		308	-6.656			308	1.072			308	-6.036		
	BCP550	288	-3.454	-48.005	-0.150	288	1.808	-12.064	-0.042	288	-3.311	-47.373	-0.155
		298	-2.016			298	-0.604			298	-2.078		
		308	-0.773			308	2.839			308	-0.244		
	FTBCP250	288	-8.320	-23.196	-0.050	288	-4.065	-50.266	-0.160	288	-6.086	-13.544	-0.025
		298	-7.909			298	-1.845			298	-6.351		
		308	-7.164			308	-0.871			308	-5.555		
	FTBCP550	288	-5.466	-41.113	-0.116	288	-3.013	-16.428	-0.047	288	-3.265	-33.886	-0.106
		298	-4.899			298	-2.286			298	-2.966		
		308	-2.975			308	-2.087			308	-1.121		
10 mg/L HAs	BCP250	288	-3.224	31.419	0.116	288	0.641	11.956	0.041	288	-2.212	22.669	0.088
		298	-5.985			298	-0.905			298	-4.716		
		308	-4.732			308	-0.118			308	-3.902		
	BCP550	288	-0.300	10.077	0.038	288	0.458	27.187	0.093	288	0.182	2.035	0.007
		298	-2.030			298	-0.890			298	-0.623		
		308	-1.258			308	-1.389			308	0.070		
	FTBCP250	288	-3.687	16.545	0.072	288	0.455	14.550	0.052	288	-2.777	16.261	0.068
		298	-6.750			298	-2.569			298	-4.713		
		308	-5.056			308	-0.465			308	-4.069		
	FTBCP550	288	-0.316	8.572	0.040	288	1.401	20.760	0.070	288	0.228	3.990	0.014
		298	-1.620			298	-1.445			298	-0.322		
		308	-0.891			308	0.107			308	-0.023		
30 mg/L HAs	BCP250	288	-1.411	49.294	0.177	288	0.864	12.371	0.041	288	-0.845	43.141	0.153
		298	-3.930			298	-0.320			298	-2.890		
		308	-4.523			308	0.083			308	-3.887		

	288	-0.506			288	0.882			288	-1.409		
BCP550	298	-1.432	21.758	0.078	298	-0.404	20.037	0.067	298	-0.497	-8.296	-0.025
	308	-1.954			308	-0.435			308	-0.946		
	288	-1.710			288	1.168			288	-1.148		
FTBCP250	298	-3.048	31.252	0.116	298	0.817	12.105	0.038	298	-2.414	35.034	0.126
	308	-4.551			308	0.407			308	-3.660		
	288	-0.785			288	0.174			288	-0.388		
FTBCP550	298	-1.748	43.931	0.156	298	-3.949	46.916	0.165	298	-1.052	17.432	0.062
	308	-3.175			308	-3.014			308	-1.625		

3.3 Asymmetrical Factorial Design for Major Environmental Impacts on POM

During combustion, whether during a wildfire or industrial pyrolysis, POM from pyrolysis temperatures ranging from 200 ~ 600 ℃ is produced, and abiotic aging may subsequently modify their surface properties. Different pyrolysis conditions and surface aging stages may form dissimilar effects of POM in TBBPA immobilization. Also, local temperatures and the competing effects of other organic matter present in the environment may play important roles in immobilization. Soil organic residues such as humic substances, for instance, are common forms of organic matter in a biomass-rich environment that may have an impact in this respect. Therefore, given that immobilization in POM can involve multiple factors and interactions, it is necessary to identify and characterize the important factors that could determine the immobilization capacity of POM as a means of exploring the nature of TBBPA immobilization in POM-rich fields.

In this context, asymmetrical factorial-assisted analysis was carried out for the purpose of better understanding and delineating five major factors during the immobilization process: presence of environmental humic substances, pyrolysis temperatures, surface aging cycles, TBBPA concentrations, and local temperatures. By using mixed-level asymmetrical factorial design and setting each parameter to low (−1), medium (0), and high (+1) or low (−1) and high (+1) values, a $2^2 3^3$ factorial design was carried out with 216 runs, including duplicated observations to estimate errors and increase the robustness in analysis of variance (ANOVA). The interactions between presence of humic substances, pyrolysis temperatures, surface aging cycles, TBBPA concentrations, and local temperatures were analyzed and any significant effects on TBBPA immobilization were identified. Given that the factors of presence of humic substances (A),

pyrolysis temperatures (B), surface aging cycles (C), TBBPA concentrations (D), and local temperatures (E) were independent variables, p-value significant levels and residual analysis were used to observe their significance with respect to TBBPA immobilization. Figure S4 shows the half-normal standardized effects that informed the identification of the significant factors and interactions in the ANOVA. The significance of the regression coefficients was determined by applying a Student's t-test. The calculated results yielded a model F-value of 57.29 ($p < 0.0001$), indicating the model is significant. The results also showed that the factors under consideration—A ($p < 0.0001$), B ($p < 0.0001$), C ($p = 0.0032$), D ($p < 0.0001$), and E ($p < 0.0001$)—are significant, as are interactions of AB ($p < 0.0001$), AC ($p < 0.0001$), AE ($p < 0.0001$), BD ($p = 0.0018$), BE ($p = 0.0476$), ABC ($p = 0.0217$), ABE ($p < 0.0001$), and ADE ($p < 0.0001$), since in each case the p-value was found to be lower than 0.05. The R^2, adjusted R^2, and predicted R^2 in this analysis were 0.9469, 0.9303 and 0.9078, respectively, indicating that the factors and interactions identified in this analysis were representative of the experimental data and therefore valid. Moreover, the adequate precision values (34.5978) were found to be above 4, indicating that these models satisfy the minimum requirement.

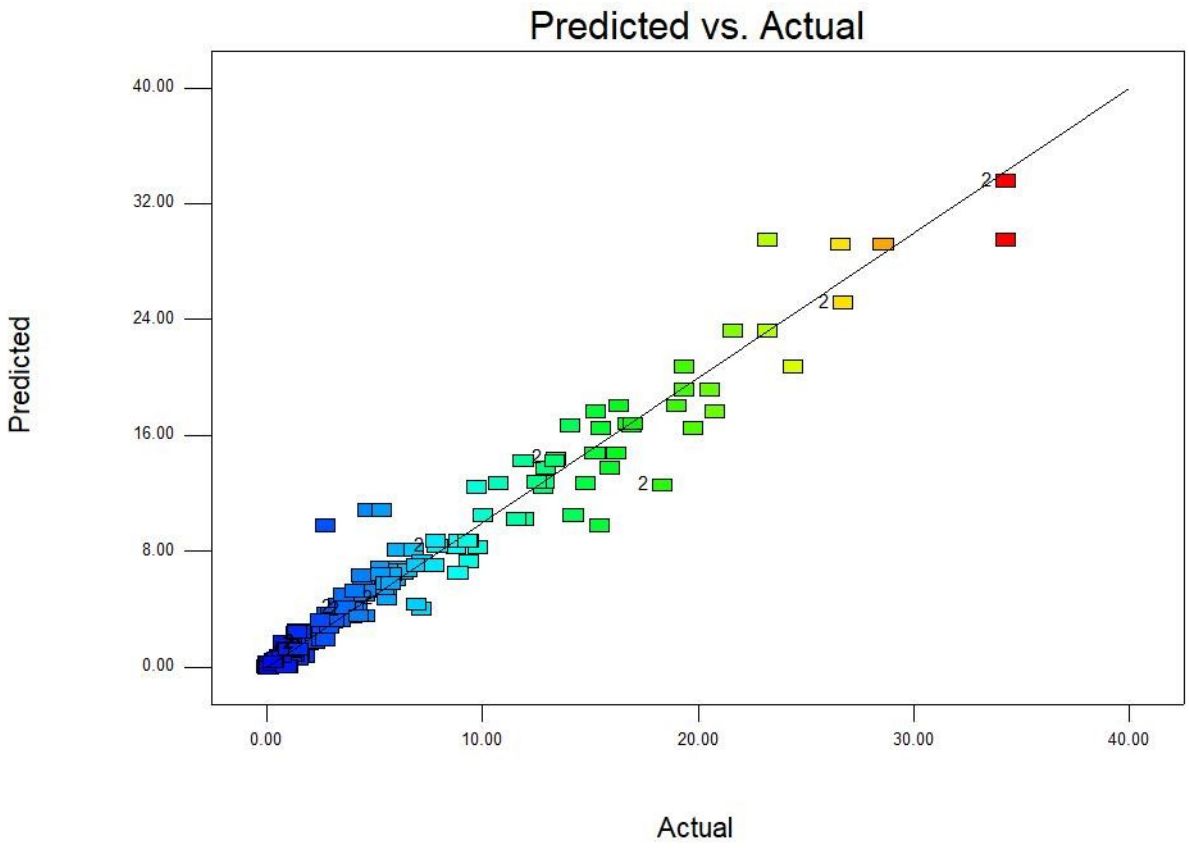

Figure.S4 The half-normal test for the factorial design

These findings indicated that all five of the factors under consideration could be considered important in TBBPA immobilization. The polyline observed in most of the three-level factors indicated that the changes in TBBPA adsorption rate were non-linear. The presence of humic substances (A), pyrolysis temperatures (B), TBBPA concentrations (D), and local temperatures (E) exhibited negative effects in terms of TBBPA immobilization in POM, while the surface aging cycles (C) showed positive effects. Referring to the isotherm studies in Figure S3, the results indicate that a lower environmental temperature, less humic substances on the POM, a low-temperature pyrolysis process, and an aged surface are favorable with respect to the adsorption of TBBPA in POM. This, in turn, suggests that TBBPA would be more readily

immobilized in regions of comparatively higher latitude and in the long-term presence of POM. The environmental behavior of TBBPA in POM was further revealed through an examination of the interactions between factors as presented in Figure 1.

The nature of the interactions between A and B suggests that the interaction can occur in humic substances with concentrations in the range of 10 ~ 30 mg/L. This, in turn, indicates that, when relatively high concentration of humic substances are present in the solution, the POM with different surface properties can specific adsorption processes in the competition adsorption of TBBPA and humic substances. The adsorption capacity of 250 ℃ pyrolyzed POM, shown to decrease as the presence of humic substances increases, was significantly affected. This may be due to humic substances favoring the surfaces of active functional groups and having stronger affinity than TBBPA on such surfaces. Also, the interaction between A and C showed that the negative effect of humic substances was boosted on surface-aged POM. The results not only show that the aging process could expose more functional groups on the surface, but also point to the slow release of TBBPA as a result of long-term presence in the environment. As indicated by the significance of the interaction between A and D, the humic substance affected the TBBPA adsorption at different TBBPA loadings, from which we can infer that humic substances together with TBBPA could contribute to a stable form of TBBPA–HA, as humic substances adsorb the TBBPA and in turn influence the POM adsorption performance. This inference is further supported by the interaction between A and E, as the favored adsorption temperature changed depending on the concentration of humic substances. The thermodynamic results shown in Table S1 indicate that the thermodynamic properties in the adsorption process were altered under the influence of humic acid (HA), suggesting that, after adding the humic substance, a different

adsorption system was formed and the immobilization mechanisms on the POM were heavily influenced. Moreover, the POM surface under different pyrolysis temperatures exhibited differences in adsorption performance with TBBPA under local temperatures and concentrations in the cases of the interactions of BD and BE. The significant differences in both performance and adsorption mechanisms could be attributable to the specific surface properties formed during the pyrolysis process. Furthermore, the interaction of DE indicates that varying local temperatures could result in different adsorption performances with varying TBBPA loading concentrations. This, in turn, suggests that, at varying temperatures and given specific TBBPA contamination levels, the POM immobilization effects on TBBPA will vary accordingly. In addition, the identification of significant interactions involving more than two factors, such as ABD, ABE, ADE, suggests that factors A, B, D, and E, could have significant combined impacts on TBBPA adsorption, implying a specific chemical path with significant driving force tied to one of these factors. Considering the unique chemical behaviors of these factors, the HA may introduce a different interactive path with respect to TBBPA.

To further investigate TBBPA immobilization in POM under various environmental conditions, and to explore the interactive behaviors of POM, the impacts and roles of nutrient ions including phosphate, nitrate, and ammonium were studied on the POM surface and aged surface, respectively, in order to gain understanding of the changes that would result from the long-term presence of POM. Thus, a two-level, three-factor 2^3 factorial design was used to determine the significant effects of environmental nutrient ions with respect to TBBPA immobilization in POM. In this study, 0.01 M and 0.001 M KNO_3, K_3PO_4, and NH_4Cl were used as a way of capturing the effects of the nutrient ions (A) NO_3^-, (B) PO_4^{3-}, and (C) NH_4^+. The impact of KCl ion

strength was studied as shown in Figure S5, which illustrates that it had little influence in the experiment and thus ion factors could be considered independent. The results in Figure 1 show that the nutrient ions had different, but in cases significant, effects on standard-surface and aged-surface POM, indicating that, under long-term abiotic aging, nutrient ions have different interactive behaviors during immobilization. Such results also imply that different types of POM have different behaviors. The significant factors and interactions with respect to NC were found to be A ($p = 0.0168$), B ($p = 0.0008$), and interaction AB (0.0264), while the significant factors and interactions with respect to LPNC were found to be A ($p = 0.0387$), and interaction AC ($p = 0.0056$). The difference in significance of these factors indicates that the abiotic aging process from NC to LPNC could alter the behavior of POM during immobilization. NO_3^- (A) showed a similar negative trend to TBBPA adsorption with respect to both NC and LPNC, suggesting that the NO_3^- had less surface-dependent effects than other factors, which may be due to its contribution to the increase in ion strength and decrease in electrostatic interactions. Meanwhile, the significant negative impact of PO_4^{3-} (B) on NCs may be due to the competition and interference with TBBPA adsorption on the surface. Compared to the relatively insignificant influence of PO_4^{3-} in LPNCs ($p = 0.1371$), the interference of PO_4^{3-} on the POM surface might have to do with the interaction with surface active functional groups, suggesting that the aged POM surface may have limited active functional groups and weakened electrostatic interactions. This result not only demonstrates that a decrease in interactions between functional groups and potential active ions could occur as a gradual process in certain environmental conditions, but also suggests that abiotic aging may alter the surface properties of POM and adopted other interactive immobilization paths. In environmental conditions, such a phenomenon may result in the slow release of nutrient ions with enhanced TBBPA immobilization for a long-term benefit in

the application of POM. Moreover, the interaction AB indicates that there was little impact when PO_4^{3-} and NO_3^- coexisted in the solution, perhaps suggesting that the NO_3^- ions prohibit the interaction between PO_4^{3-} and the POM surface by decreasing electrostatic interaction. This result further supports the inference that the effects of NO_3^- and PO_4^{3-} were due to the electrostatic properties on the surface of the POM, and that these properties, in turn, may be a function of the surface structure and functional groups. In addition, on LPNC, the significant interaction of AC suggests that the addition of both NO_3^- and NH_4^+ could cause notable negative effects in TBBPA immobilization. It was also observed that the aged POM surface had negative sites for NH_4^+ adsorption while the NO_3^- repulsed weak electrostatic interactions of TBBPA, thereby inhibiting TBBPA adsorption due to the interferences of electrostatic interactions. This observation suggests that abiotic aging may alter the surface of POM, forming inactive functional groups for weak electrostatic interactions, which in turn may ultimately reduce its capacity for TBBPA immobilization. On the other hand, in POM sites, the introduction of agents that primarily consist of NO_3^- and NH_4^+ (e.g., fertilizers) could cause the release of immobilized TBBPA in long-term existing POM, resulting in potential secondary soil pollution in the form of TBBPA.

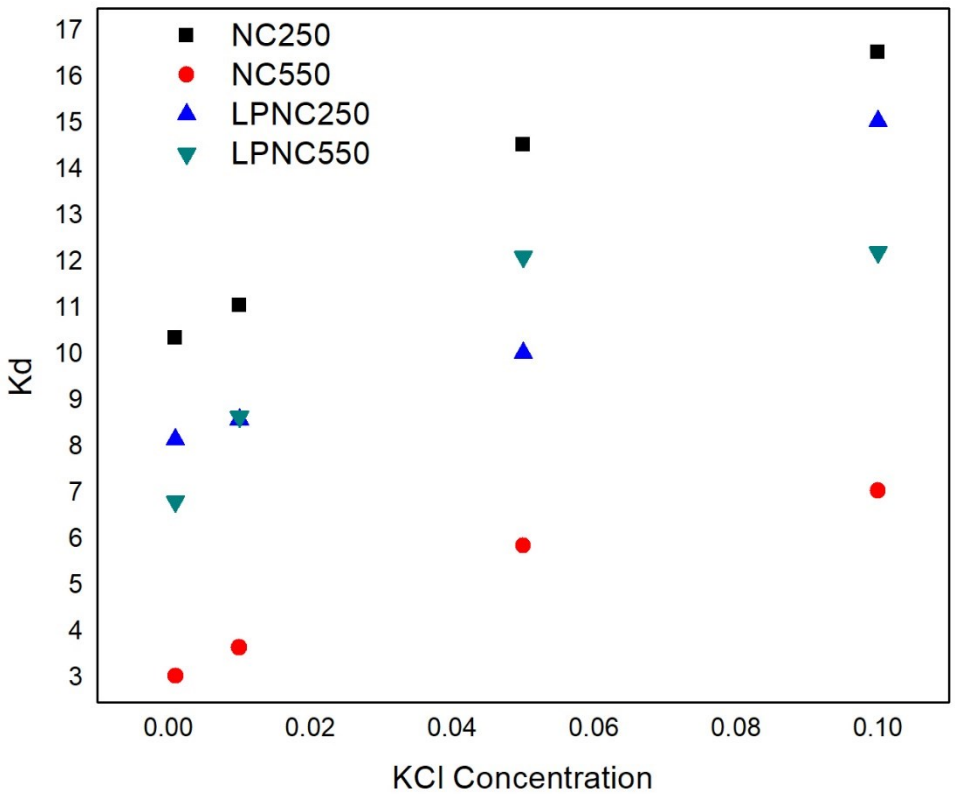

Figure S5. Effect of KCl concentration for adsorption of TBBPA on POMs

3.4 Surface Alterations during Abiotic Aging

To identify alterations due to abiotic aging, the surfaces of different types of POM were characterized through various approaches. SEM and AFM analyses were conducted in order to observe changes in surface geometry structures at scales ranging from micro to nano. Figure S6 shows that, according to the SEM results (Figure.S8), the surfaces of the different types of POM were found to have been substantially altered under different treatments in pyrolysis and abiotic aging conditions. Under pyrolysis temperatures ranging from 250 ℃ to 550 ℃, the surfaces of

the POM particles were converted from a flat-, smooth-layered surface to a compact shell integrated with pores distributed on valleys and channel tubes crossing on its sides. This indicates that the pyrolysis process consists of heterogeneous alteration of the POM, where the surface pores are altered in different directions. Moreover, at a nano scale, the AFM results show no obvious differences between the different types of POM under various pyrolysis conditions. The NC250 and NC550 POM was found to feature irregular surfaces with “antenna-like” peaks, possibly indicative of active performance in interactions. The LPNCs, however, instead of a cracked surface with cracks extending in all directions as in the case of the NCs in SEM, had a flat and silky surface after abiotic aging. Such results indicate that, during the abiotic aging process, the freeze-thaw cycles serve to not only curve the surface fissures observed in the macroscope, but also break down the nanoscale peaks, which may result in an alteration of the physicochemical properties of the POM.

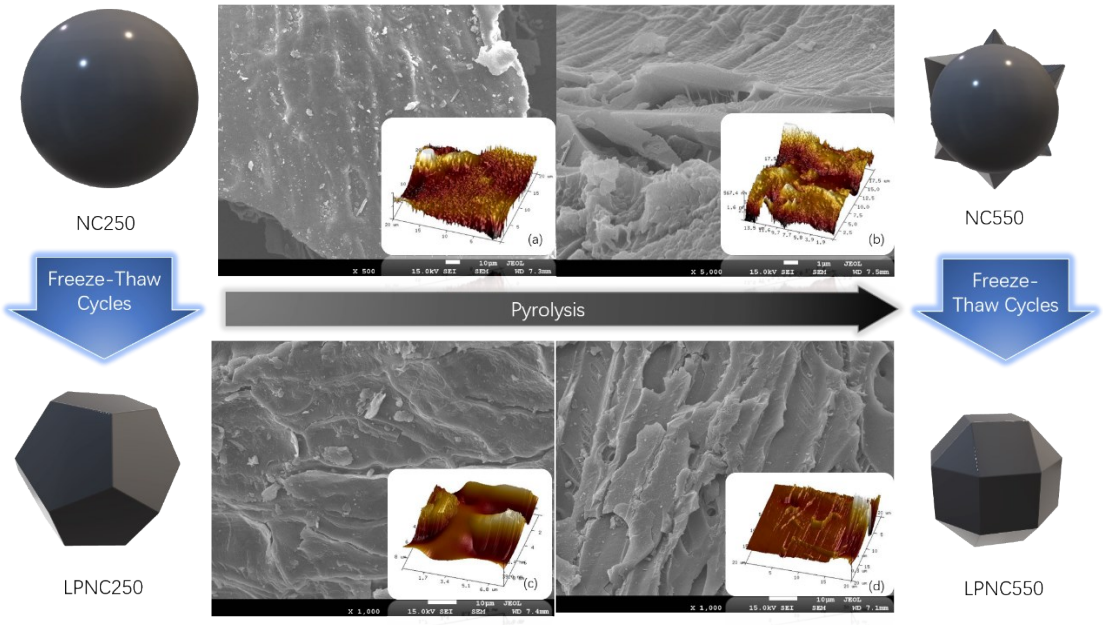

Figure. S6 The atomic force microscope images for carbon surface on (a)NC250, (b)NC550,

(c)LPNC250, and (d) LPNC550

In addition, to confirm that the abiotic aging process had in fact altered the chemical composition of the POM, synchrotron-based FTIR analysis was carried out for the purpose of analyzing the changes in surface functional groups. TBBPA and HA were also added in order to investigate their specific interactions under the impact of surface changes. Figure S7 shows the obvious differences observed between NC250 and LPNC250, where 1,230 cm^{-1} ~ 1,260 cm^{-1} of O—H bending[41, 42] were significantly altered, indicative of the impact of aging on the hydroxyl groups. Although there were no significant changes between NC550 and LPNC550, peak shifts were also observed in the range of 1,100 cm^{-1} ~ 1,000 cm^{-1} for the ester and hydroxyl bands. This is notable because such changes in oxygen-containing groups may lead to changes in the chemical interactions with TBBPA and HAs. Furthermore, the specific interaction of hydrogen bonds could be reflected in the results in the range of 1,100 cm^{-1} to 1,000 cm^{-1} with specific peaks in different types of POM. For example, the sharp peaks observed at 1,080 cm^{-1}, 1,075 cm^{-1}, and 1,060 cm^{-1} had high intensities with respect to NC550. Nevertheless, for LPNC550 with the introduction of HAs, only the wide peak at 1,060 cm^{-1} remained. Meanwhile, the significant variances between NC250 and LPNC250 suggest that the sharp peaks around 1,060 cm^{-1} were altered differently by TBBPA compared with HA, and exhibited different peaks (at 1,075 cm^{-1}, 1,052 cm^{-1}) in LPNC250, and peaks of 1,062 cm^{-1} and 1,043 cm^{-1} in NC250. The altered and shifted peaks suggest that alterations of the POM surface as a result of aging could influence the interactions with contaminants and DOM. As such, the results show that freeze-thaw cycles significantly alter the surface groups of POM, where the POM produced at relatively low temperatures in particular could be significantly affected by the freeze-thaw cycle.

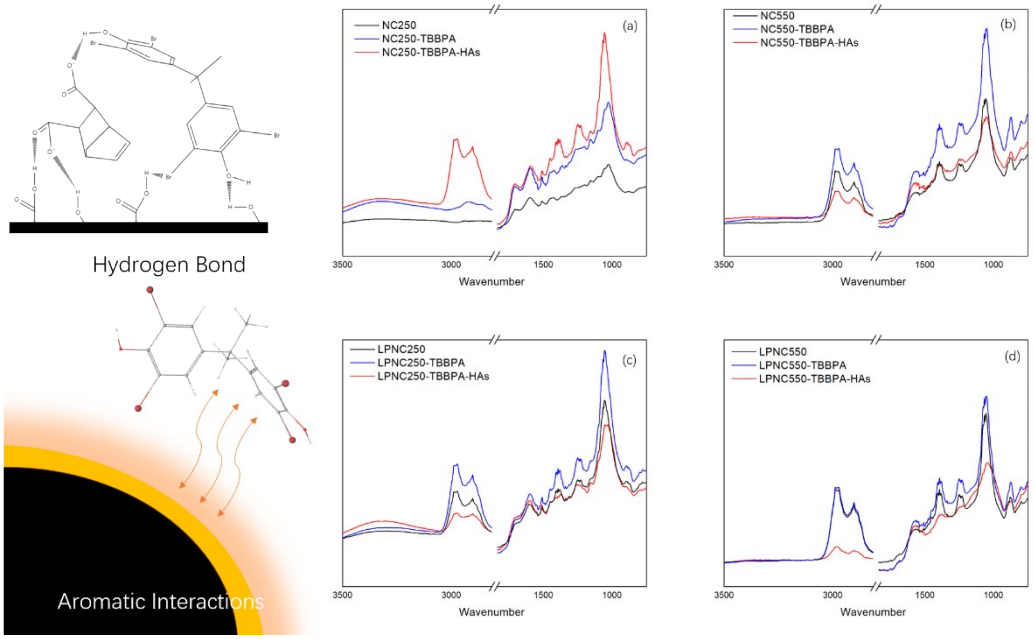

Figure.S7 The Synchrotron-based FTIR analysis on the surface of: (a) NC250, (b) NC550, (c) LPNC250, and (d) LPNC550, under the influences of TBBPA and HAs

S3.5. SEM Analysis for POM during the Freeze-Thaw Aging

SEM analysis of pyrogenic carbon was conducted to determine the surface geometry structure and porosity. The results are shown in Figure. S8, which exhibited the surface geometry structure changed after physical aging. The difference also existed for the pyrogenic carbon produced from different pyrolysis temperatures. NC250 showed a flat layered structure with smooth and distinct hollow distributed on surface. NC550 showed an integrated compact structure with numerous pores distributed with valleys and channels. After physical surface aging, the surface of LPNC250 displayed fold and wrinkled debris divided by curved grooves, indicating the cracking damage induced by freeze-thaw process. In comparison, the aged surface of LPNC550 exhibited more pores with rough layers.

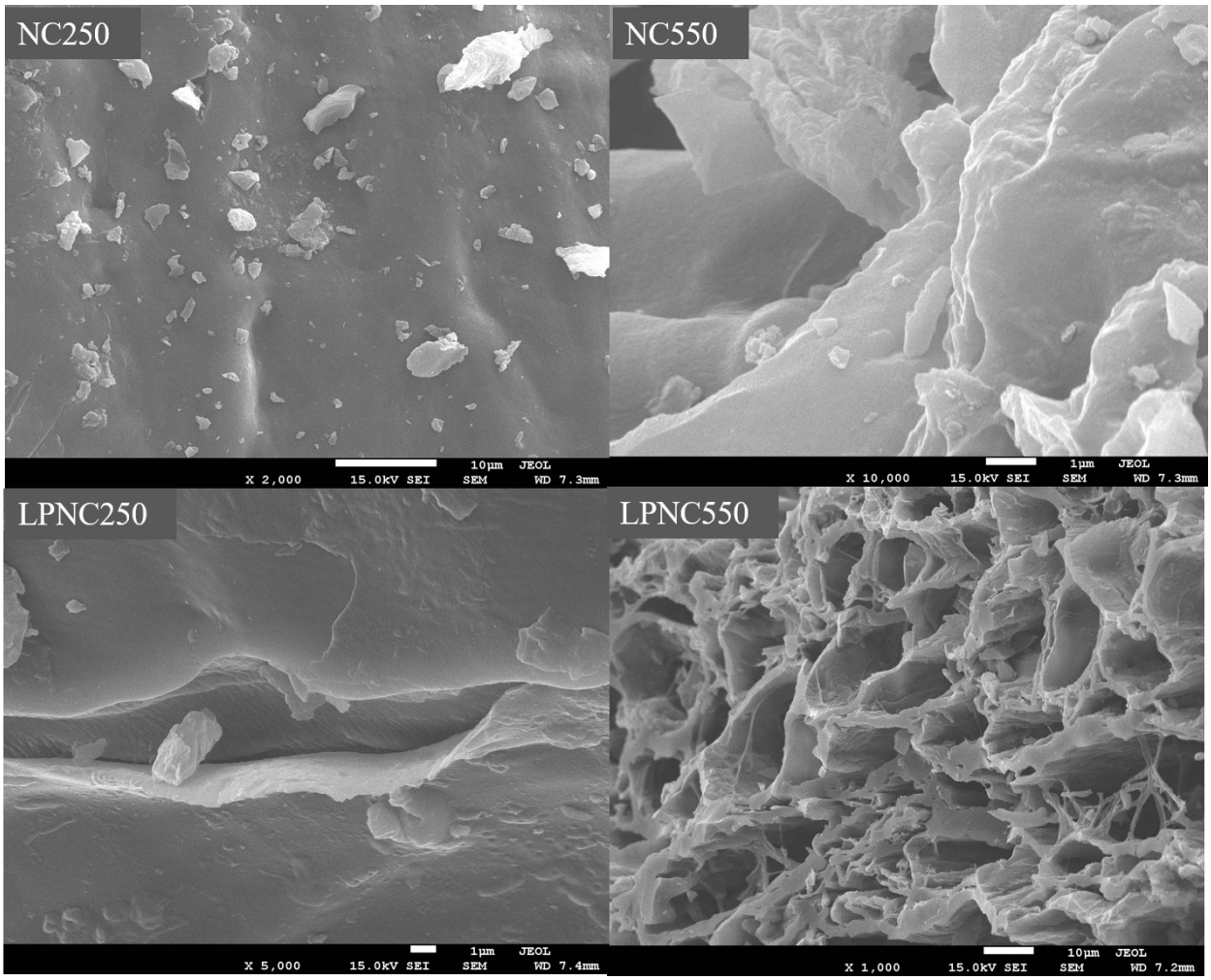

Figure.S8. Scanning electron microscope images of pyrogenic carbon surfaces

S3.6 Adsorption/Desorption Kinetics and Tolerance of Humic Acids

A study of the adsorption kinetics not only helps with estimating the adsorption performance of TBBPA immobilization in POM, but also provides information with respect to the mechanism of surface adsorption via the kinetic models. As such, in our study different temperatures were with respect to adsorption kinetics to order to capture the effects of local temperatures during TBBPA immobilization. A time-dependent desorption analysis was also studied for the purpose of

exploring the TBBPA slow-release process.

Employing pseudo-first-order, pseudo-second-order and intraparticle diffusion models, the rate-controlling mechanism for TBBPA adsorption was determined and investigated. The Lagergren pseudo-first-order kinetics model, it should be noted, can be expressed as:

$$Q_t = Q_e(1 - e^{-k_1 t}) \quad (7)$$

where Q_t (mg/g) represents the amount of adsorbate adsorbed at a predetermined time, t (min), Q_e (mg/g) is the amount of adsorbate adsorbed at equilibrium, and k_1 (1/min) is the rate constant.

The Lagergren pseudo-second-order kinetics model is defined as:

$$Q_t = \frac{Q_e^2 k_2 t}{1 + Q_e k_2 t} \text{ and } h = k_2 Q_e^2 \quad (8)$$

where k_2 (g/mg min) is the pseudo-second-order rate constant and h (mg/g min) is the initial adsorption rate.

An intra-particle diffusion rate model helps to determine the rate-controlling step, understood as pore diffusion in an adsorption mechanism. This can be described as:

$$Q_t = k_p t^{0.5} + C \quad (9)$$

where k_p (mg/g min0.5) is the intra-particle diffusion rate constant and C (mg/g) is a constant that describes the boundary layer effect. Here, higher C values are indicative of a higher boundary layer effect and thus are descriptive of the inapplicability of pore diffusion as the sole

rate-determining step in describing the dynamics of the adsorption process. If $C = 0$, the adsorption kinetics are controlled only by intraparticle diffusion. If $C \neq 0$, the adsorption process is highly complex.[11] In our case, parameter C was found to increase with a corresponding increase in k_1, k_2 and h, a phenomenon that may be attributable to the increase in thickness of the boundary layer in turn resulting in an increase in adsorption rate.

The Elovich model describes chemisorption on a solid surface and a decrease in adsorption velocity due to the covering of the superficial layer, [12] phenomena that can be expressed as:

$$Q_t = \frac{1}{\beta} log_e(\alpha\beta) + \frac{1}{\beta} log_e(t) \quad (10)$$

where α is the initial adsorption rate (g/(mg min)), and β is the desorption constant (g/mg). [13, 14]

3.7 Time-Dependent Desorption Kinetics of TBBPA Released from POM

Considering that the *k* values from the adsorption process can be easily influenced, the release of POM could also be affected. Therefore, in order to estimate the long-term immobilization performance of POM, the desorption process in the presence of DOM was likewise analyzed. Figure 2 indicates that the desorption process occurred after relatively long-term immobilization of TBBPA. By investigating the time-dependent desorption process, a desorption kinetic was obtained using the pseudo-first-order kinetic model. The results show that, under rapid shaking, the adsorbed TBBPA became detached, and then the system subsequently achieved rebalance after 160 min. After 250 min, a few adsorbed TBBPA could be found desorbed in the system,

indicating that the system had reached rebalanced equilibrium. With the different types of POM under various conditions, in general the desorption occurred rapidly during the first 100 min, and gradually met the equilibrium within about 250 min. Following abiotic aging, it was found that the aged POM had an increased release capacity compared with the original POM. For instance, NC250 and NC550 had relatively low desorption rates (C_t/C_0), at 1.47 and 1.22, respectively, compared with LPNC250 (3.53) and LPNC550 (1.46), indicating that the release of TBBPA was greater in aged POM than in fresh POM. In particular, a notable change in desorption rate was observed between NC250 and LPNC250 from 1.47 to 3.53. This change was due to surface alterations during abiotic aging. Although the porous surface was improved as a result of abiotic aging, the surface chemical properties, including active functional groups, were deactivated, and the stability of TBBPA immobilization was also weakened.

In addition, DOM was found to promote the desorption performance of both release speed and rate. Compared to the non-DOM condition, in most cases the desorption under DOM reached equilibrium at 80 min (compared to 160 min in the case of the non-DOM condition), indicating that a more rapid desorption process had occurred. Table S3 also shows that the kinetic constants of the DOM solutions increased, e.g., NC250 and LPNC550 increased from 0.014 L/min and 0.016 L/min, respectively, to 0.039 L/min. Therefore, aside from adsorption, DOM also exhibited significant impacts on the desorption process with an increase in desorption performance. These results also imply that NC250 and LPNC550 surfaces could share similar properties, as only minor changes in adsorption rate could be observed on NC250 and LPNC550, and they had similar desorption curves with/without DOM. NC550 and LPNC550 also had similar curves and similar degrees of decrease in desorption kinetics, indicating that they could

have similar desorption behaviors that are different from the shared desorption path of NC250 and LPNC550. Based on these observations, the curve of NC250 and LPNC550 was labeled “L-type” curve groups, while the NC550 and LPNC250 curves were designated “C-type” curve groups. These results indicate that POM surfaces modified by pyrolysis and by abiotic aging may share properties related to their function in interfering with the transport of TBBPA.

Table.S3 *k*-Values of Different Kinetic Models during TBBPA Immobilization

Temperature (K)		Adsorbent	Pseudo-first-order			Pseudo-second-order				Intra-particle model			Elovich model		
			$Q_{e\,cal}$/(mg/g)	k_1 (L/min)	R^2	$Q_{e\,cal}$/(mg/g)	k_2 (g/mg min)	h	R^2	k_p (g/mg $min^{0.5}$)	C	R^2	α (g/mg min)	β (g/mg)	R^2
288	Non-DOMs	NC250	2.053	0.011	0.989	2.294	0.006	0.031	0.986	0.360	0.062	0.785	0.070	2.270	0.964
		NC550	1.517	0.006	0.993	1.790	0.004	0.011	0.983	0.099	0.048	0.869	0.032	2.932	0.961
		LPNC250	2.011	0.008	0.980	2.273	0.004	0.023	0.985	0.303	0.060	0.858	0.066	2.412	0.971
		LPNC550	1.764	0.008	0.993	2.026	0.004	0.018	0.996	0.213	0.054	0.873	0.047	2.590	0.985
	DOMs	NC250	1.177	0.114	0.931	1.219	0.172	0.256	0.972	0.747	0.019	0.422	645.823	12.467	0.997
		NC550	0.942	0.035	0.838	1.005	0.049	0.050	0.964	0.515	0.017	0.744	0.378	7.622	0.952
		LPNC250	1.202	0.077	0.882	1.266	0.091	0.146	0.952	0.668	0.024	0.576	8.946	8.402	0.995
		LPNC550	1.010	0.034	0.957	1.077	0.045	0.052	0.992	0.437	0.023	0.635	0.360	7.000	0.951
298	Non-DOMs	NC250	1.856	0.068	0.949	1.938	0.058	0.218	0.991	1.074	0.032	0.454	26.946	5.954	0.960
		NC550	1.215	0.107	0.973	1.248	0.176	0.273	0.956	0.815	0.016	0.257	23127.026	15.460	0.908
		LPNC250	1.894	0.065	0.967	1.976	0.055	0.213	0.997	1.087	0.033	0.454	23.061	5.757	0.957
		LPNC550	1.717	0.058	0.982	1.790	0.053	0.171	0.983	0.965	0.030	0.423	12.293	6.072	0.904
	DOMs	NC250	1.783	0.025	0.903	1.905	0.020	0.071	0.970	0.682	0.043	0.726	0.376	3.687	0.975
		NC550	1.155	0.076	0.916	1.209	0.101	0.148	0.978	0.669	0.021	0.497	18.908	9.571	0.987
		LPNC250	1.657	0.060	0.960	1.739	0.053	0.162	0.995	0.908	0.031	0.504	7.634	5.920	0.959
		LPNC550	1.429	0.033	0.936	1.523	0.031	0.073	0.988	0.616	0.033	0.662	0.532	4.992	4.992
308	Non-DOMs	NC250	1.558	0.098	0.956	1.613	0.114	0.296	0.992	0.995	0.024	0.371	876.384	9.546	0.981
		NC550	0.707	0.112	0.948	0.733	0.282	0.152	0.983	0.454	0.011	0.390	563.845	21.373	0.993
		LPNC250	1.772	0.096	0.976	1.828	0.102	0.342	0.997	1.154	0.026	0.319	2680.584	9.049	0.964
		LPNC550	1.028	0.069	0.986	1.064	0.117	0.133	0.988	0.622	0.016	0.362	53.320	12.240	0.918
	DOMs	NC250	1.914	0.050	0.914	2.019	0.038	0.154	0.978	0.974	0.039	0.589	3.322	4.563	0.976
		NC550	1.312	0.102	0.981	1.349	0.156	0.284	0.995	0.875	0.018	0.283	11552.751	13.668	0.960
		LPNC250	1.965	0.045	0.951	2.067	0.034	0.146	0.989	0.994	0.039	0.546	2.907	4.407	0.949
		LPNC550	1.688	0.062	0.992	1.759	0.059	0.182	0.992	0.972	0.029	0.407	19.778	6.481	0.913

3.8 Immobilization of Ionized TBBPA Species on POM Surfaces after Abiotic Aging

The electrostatic properties of different types of POM can be revealed in the interactions with ionized TBBPA species. The ionized species of TBBPA, in turn, can play an important role in TBBPA immobilization, as they often have different hydrophobicity/hydrophilicity and specific chemical structures. In particular, TBBPA-ionized species may interfere with TBBPA immobilization in POM, since the ionized TBBPA could interact with the functional groups and porous interfaces on carbon structures of POM due to the changes in hydrophobicity/hydrophilicity and specific functional groups during ionization. In our study, by altering the pH in the solution, TBBPA transformed to different species, including $TBBPA^0$, $TBBPA^-$, and $TBBPA^{2-}$ (Figure S9). Accordingly, the adsorption of different TBBPA species was derived as shown in Figure S10. The results show that NC250 and LPNC250 had generally high adsorption rates for all species of TBBPA, indicating high immobilization capacity on POM surfaces to both the molecular form of TBBPA ($TBBPA^0$) and the ionized forms of TBBPA ($TBBPA^-$ and $TBBPA^{2-}$). This further suggests that a POM surface with rich activity of surface functional groups is favorable for all forms of ionized TBBPA. In addition, the immobilization of ionized TBBPA (both $TBBPA^-$ and $TBBPA^{2-}$) takes a lower amount of adsorption than $TBBPA^0$, indicating that the major species of TBBPA immobilization in POM are TBBPA molecular forms, as well as that a pH below 7 is favorable. However, in the pH range of 5 to 8, the pH impacts on adsorption performance were found to increase for NC250 and LPNC250, whereas other forms of NC550 and LPNC550 POM exhibited low but steady adsorption rates. LPNC550, as well as NC250 and LPNC250, also exhibited an increased adsorption rate to $TBBPA^{2-}$. While different with NC250 and LPNC250, LPNC550 had a relatively low immobilization capacity to

$TBBPA^0$ and $TBBPA^-$. Given that $TBBPA^{2-}$, an extensively ionized organic compound, is dominated by electrostatic interactions, the low adsorption on LPNC550 could be explained by the fact that, after abiotic aging, LPNC550 could be exposed to weakened negatively charged surface, a situation favorable to $TBBPA^{2-}$ ions. Such a phenomenon may also be what occurred on the surface of the LPNC250, as the adsorption of ionic TBBPA was higher for LPNC250 than for NC250. Such results support the inference that abiotic aging in POM not only deactivates the unstable functional groups, but also weakens the negatively charged sites on the surface. Moreover, we note that, after the introduction of DOM, the adsorption of $TBBPA^{2-}$ ($K_d = 0.38$) was higher than the adsorption rate in non-DOM ($K_d = 0.21$), especially on LPNC250. This result supports the inference that TBBPA in DOM solutions has a different adsorption process for forming TBBPA–DOM cohesion, suggesting that there could be a particular DOM–$TBBPA^{2-}$ ionic form that takes shape in higher pH ranges, and that the cohesion of TBBPA–DOM could also affect the adsorption of other, less favorable, TBBPA forms, such as DOM–$TBBPA^-$ and DOM-$TBBPA^0$. Furthermore, in the DOM solutions, the immobilization behavior of the three species of TBBPA not only decreased, but also changed (as demonstrated by the differing adsorption curves). In particular, the adsorption was altered to clearly exhibit the single adsorption peak of $TBBPA^-$ in POM (in contrast to the double peaks in non-DOM solutions). For $TBBPA^0$, a distinguishable peak appeared in the DOM solution with all types of POM when the pH was within the range, 6 ~ 6.5. These results further support the inference that the presence of DOM can alter the adsorption mechanisms while decreasing the adsorption rate. Moreover, the modified adsorption mechanism is likely to exhibit dissimilar transport behavior in the environment.

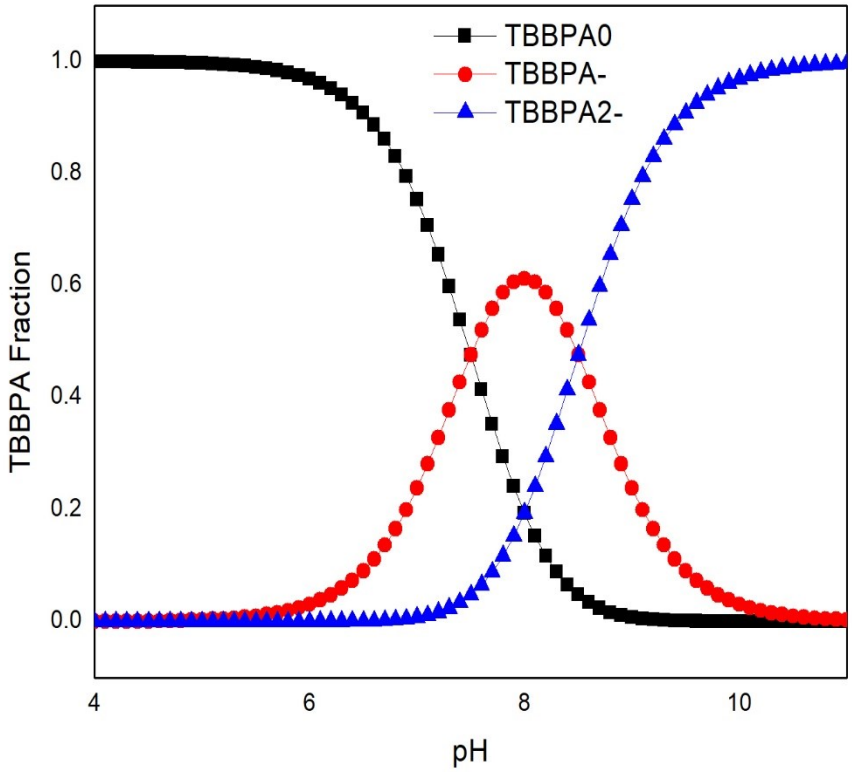

Figure.S9. The distribution of TBBPA species in the pH ranges

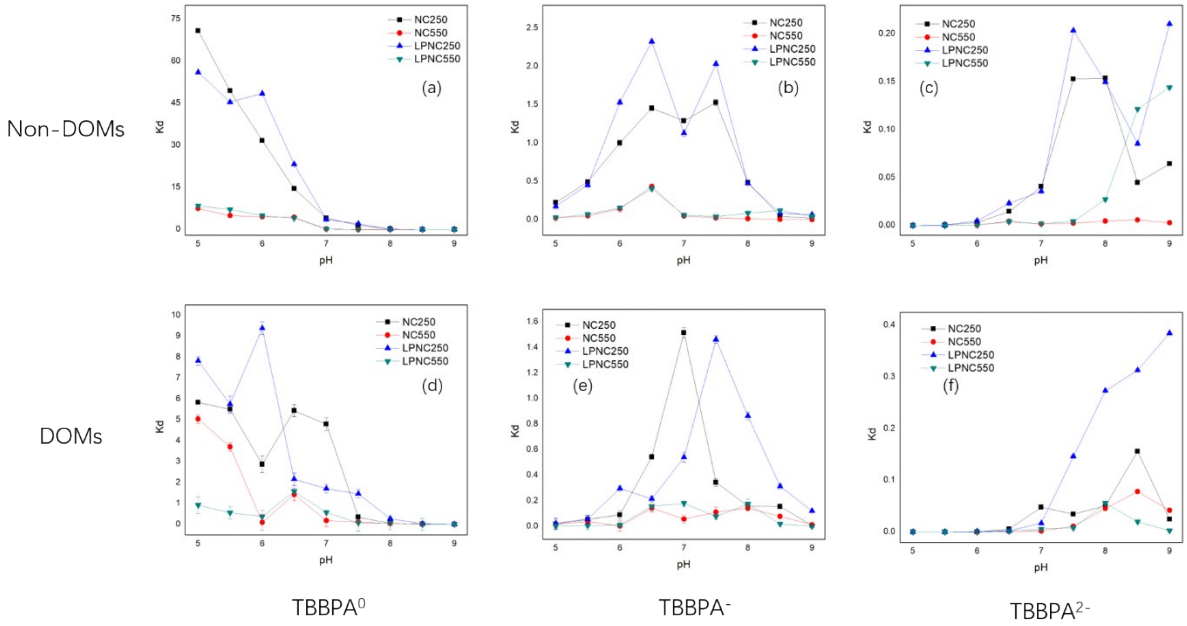

Figure.S10 The immobilization of TBBPA species on POMs

Furthermore, in POM fields, the immobilization of ionic TBBPA in non-DOM/DOM conditions can also represent their transport behaviors in environmental circumstances, since ionized compounds can facilitate the transport process. Ostensibly, the transport of all TBBPA may be contained within an acidic region. Furthermore, the long-term application of POM is shown to be correlated with higher immobilization capacity for all forms of TBBPA, indicating that, after long-term development of a POM-rich site, the TBBPA transport could be reduced. Moreover, during the long-term aging process, the augmented higher adsorption rate could also cause local POM to accumulate TBBPA. In DOM-rich areas, although immobilization capacity may diminish, TBBPA transport could still be reduced through the long-term presence of POM, where the transport of $TBBPA^{2-}$ is limited. In other words, the transport of TBBPA may decrease in alkaline regions in favor of a transport path more consistent with those of $TBBPA^{0}$ and $TBBPA^{-}$.

3.9 Synchrotron-based SD-FTIR analysis on physical aged carbons

the notable differences are found between NC250 and LPNC250 (Figure.S11 and Figure.S12), indicating the changes of surface functionality after physical aging. The peak changes close to 1750, 1400, 1250, 1080, 1020 and 880 cm-1, indicates that alkene branches, aromatic structures and unsaturated oxygen-containing groups are affected, respectively. Strong responses of v(C=CH2) and v(C—H) at 890, 880 and 860 cm-1 are observed in LPNC250. The strong peaks at 1400, 1380 and 1370 cm-1 for C—H bending of alkene represent that the surface of FTBCP250 has predominated aromatic structures. Although LPNC250 also presents active hydroxyl groups of similar response at 1150 cm-1, the responses of functional groups in the range from 1300 to 1000 cm-1 are altered. After physical aging, specific weak oxygen containing groups related to stable aromatic structures are enhanced while most of oxygen containing groups are decreased, resulting in the decrease of variety in functional groups. The medium response at 1050 cm-1 on NC250 splits into two very strong responses at 1060 and 1040 cm-1 in LPNC250, indicating the changes in symmetry of surface complexes.[15] Therefore, as shown in Figure. S9, from the view of surface functionality, a “homo-functionalization” process can be used to describe the surface structure development in physical aging process through the consolidation of oxygen containing groups with aromatic structures and antagonization of other active hydroxyl groups.

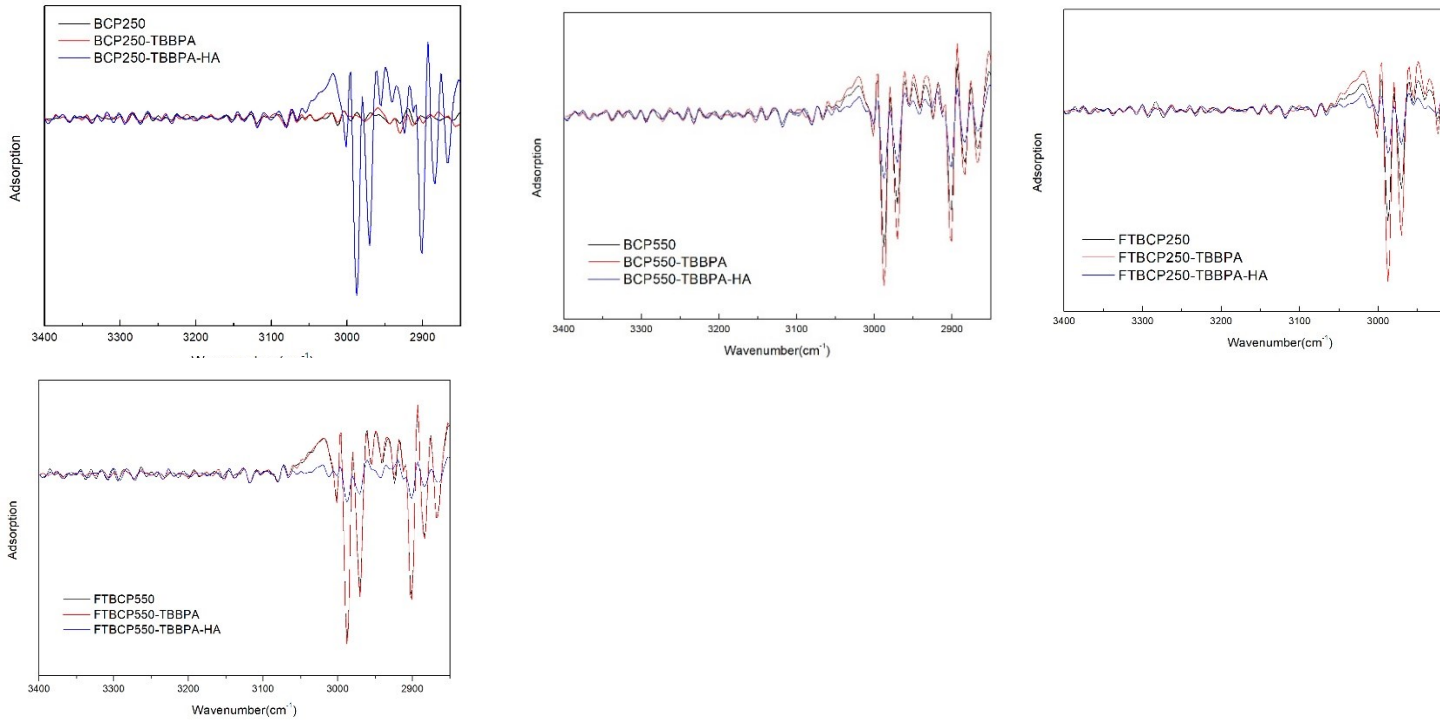

Figure. S11 SR-SD-FTIR analysis on 3400-2900 cm-1

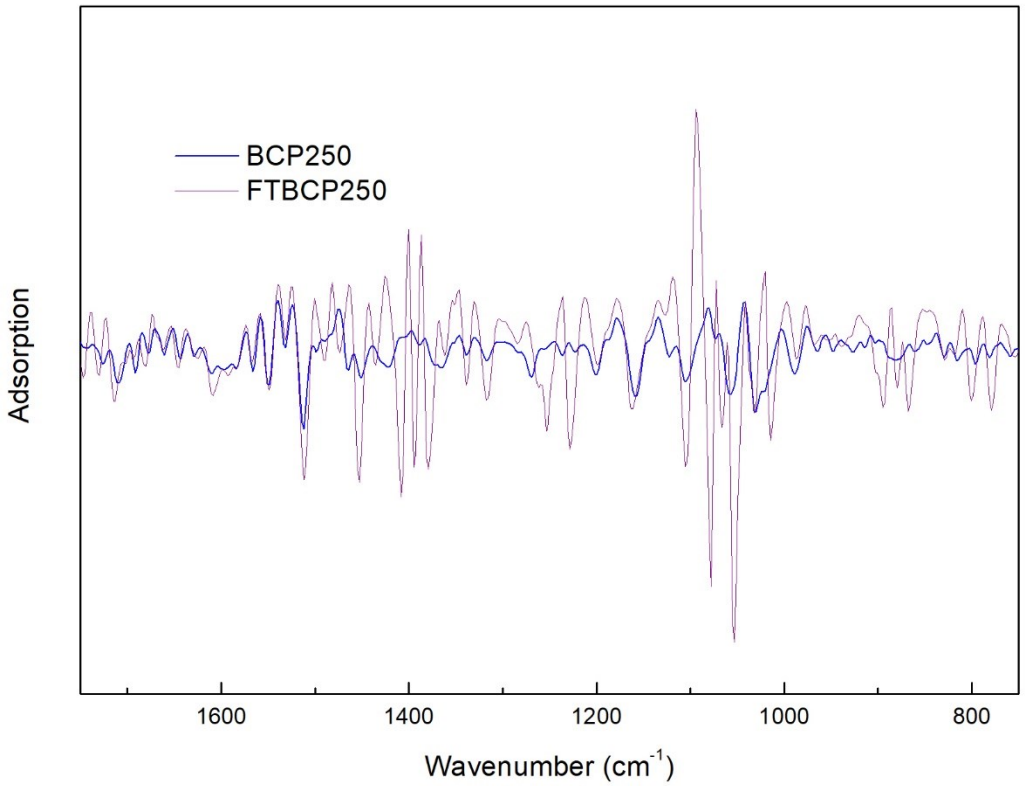

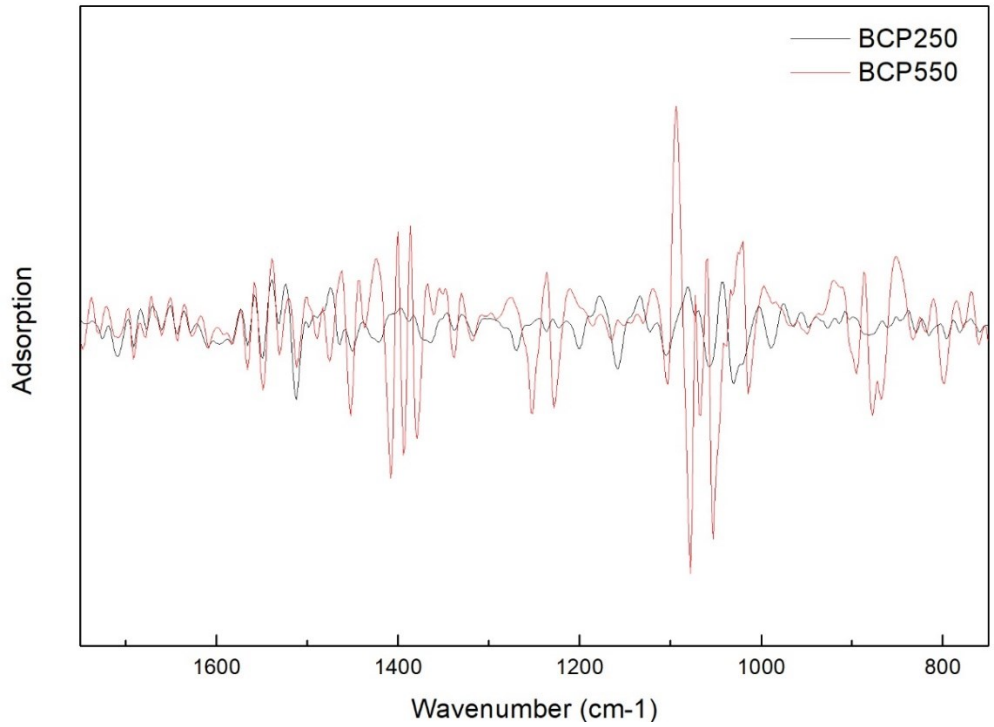

Figure.S12 Changes from pyrolysis and physical aging process

3.10 Synchrotron-Based FPA FTIR Analysis

SR-FPA-FTIR was further used to analyze the distribution of function groups and structures on the surface of pyrogenic carbon. Figure. S13 showed that the mapping results of FTIR responses in the wavenumber of 1200-1100 cm^{-1} to estimate the distribution of unstable/active hydroxyl groups. NC250 exhibited strong and widely distributed results. Combined with the SR-SD-FTIR results of multiple responses in 1200-1100 cm^{-1}, the carbon derived from low pyrolysis temperature had a number of unstable/active hydroxyls spreading on the surface, which played an important role in the interactions with TBBPA. Besides, as the response was reduced in LPNC250, the homo-functionalization process in physical aging not only changed the compositions but also influenced the distribution. Furthermore, as the distribution of the unstable/active hydroxyls in LPNC250 was mostly on the ridge, the homo-functionalization process might be generated due to the damage of the shallow surface, which that had multiple active hydroxyls from low pyrogenic carbon. Then the surface was corrupted deeper and exposed carbon structures of fine pyrogenic carbon with stable and uniformed structures. In addition, the low contents of hydroxyls on NC550 and LPNC550 exhibited insignificant difference, due to their high pyrolysis temperature.

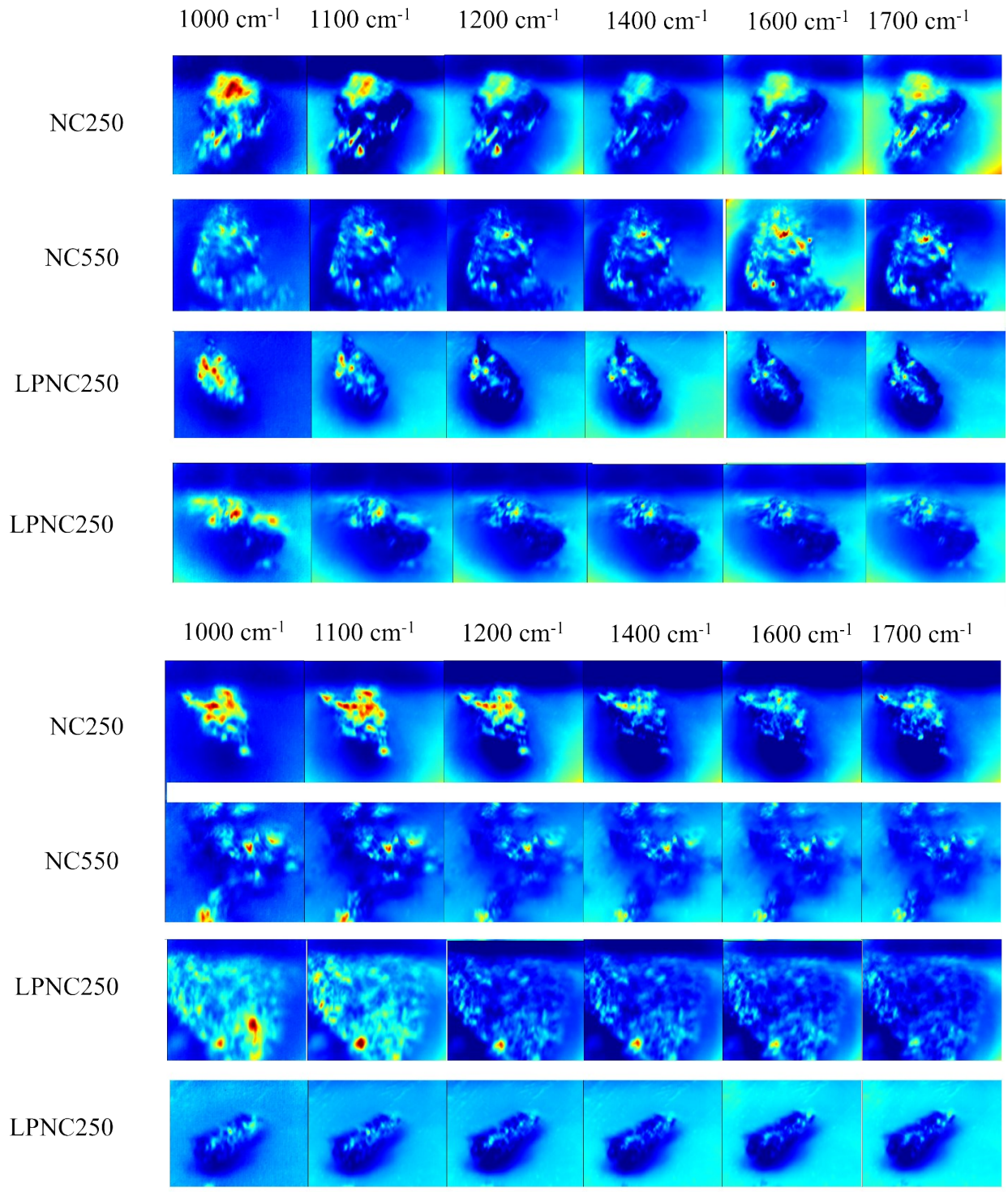

Figure. S13. Synchrotron-based FPA-FTIR analysis of pyrogenic carbon surfaces in different wave numbers with (a) involvement of TBBPA, and (b) involvement of TBBPA and HAs.

In Fig. 13(b), shifts of distribution were observed on the pyrogenic carbon surface with NOMs and TBBPA. The significant changes displayed in the range of 1100~750 cm^{-1}, indicating varied hydroxyl interactions. Compared to the results with only TBBPA on pyrogenic carbon, the distribution shifts of hydroxyl groups were due to the competing adsorption of TBBPA and NOMs on carbon surface. Moreover, NC250 exhibited high response and dramatic changes of hydroxyl distribution with other oxygen containing groups. It suggested the active hydroxyl groups on low-temperature pyrogenic carbon surface were sensitive in the interactions with TBBPA and NOMs. Meanwhile, LPNC250 showed the different distribution of C—H, C=C and C—O, indicating different adsorbates were attached at the sites. BCP550 and FTBCP550 both exhibited relatively low response and uniformed distribution, which were attributed to the low adsorption rate of TBBPA resulting from the coverage of NOMs. Therefore, NOMs and TBBPA might favor different sites, but both were sensitive to active hydroxyls.

3.11 Synchrotron-Based FPA FTIR Analysis on Phototoxicity

To highlight the alterations of the functional groups on the surface, the invert signal of processed results was applied. Figure 3 shows that the samples from fresh POM had comparably higher intensities (in the range of 1,000 ~ 1,100 cm^{-1}) than both the aged POM and the regular soil. The functional groups in this range were attributed to hydroxyl groups that were able to interact with TBBPA[22], indicating that, during the growth of vegetation, the medium mix with fresh POM may maintain the interaction with the TBBPA, meaning that the TBBPA would remain on the

surface of the POM. In addition, in the range of 1,500 ~ 1,600 cm^{-1}, the samples from aged POM showed relatively high density of signals, a finding indicative of the distribution of aromatic structures and carboxyl groups. Such results not only signify the presence of POM, but also imply that the carboxyl groups on fresh POM may be altered during the growth of the vegetation, as the fresh POM was found to have aromatic structures similar to those of the aged POM, but with fewer signals after the growth stage. Moreover, the regular soil had strong intensity (in the 1,600 ~ 1,700 and 2,900 ~ 3,000 ranges), attributable to the C=O groups in the SOM[48], and suggesting that the SOM remained on its surface. In terms of nutrient utilization by the vegetation, our results indicate that, despite the influence of TBBPA, the vegetation with POM may still have higher utilization of SOM than does the regular soil. This conclusion is supported by the enhanced growth state of the specimens in the presence of POM by the end of the observation.

Thus, though the polluted POM was found to increase the growth of the vegetation without inhibiting the transferal of nutrients, under the influence of POM, the vegetation exhibited vulnerability to the toxic effects of TBBPA, indicating that, when contaminated by organic pollutants, sites with POM may sustain higher damage to local flora. Moreover, although the aged POM had relatively higher adsorption performance than the fresh POM, the impact was observed to be significantly lower than that of fresh contaminated POM, indicating that POM could in the long term reduce the transfer of TBBPA to vegetation. Furthermore, in light of the constant impact of fresh POM after 95 days of observation and the TBBPA-related groups found on their surface as observed in our study, the long-term toxic exposure of the local environment due to the slow release of TBBPA contaminants prior to aging was identified as a significant

hazard, especially for regions with a mild climate where frequent freeze-thaw cycles are not likely to occur.

The immobilization of TBBPA contaminants in POM could produce uncertain impacts on the local environment. Considering the ubiquity of POM in the natural environment and the wide application of pyrolysis, adsorbed TBBPA in POM may have an impact on pyrolyzed sites and be detrimental in the long term to local species. Therefore, an exploration of the positive/negative impacts of such immobilization is needed. To investigate the joint long-term effects of POM and TBBPA on the environment, a series of pot experiments were carried out. As a common species which appears in most ecosystems, especially near wildfire sites or residential areas, tall wheatgrass (*Thinopyrum ponticum*) was introduced as a target flora species in order to explore the positive/negative impacts of POM–TBBPA. Figure 3 shows that the growth of tall wheatgrass was enhanced through the addition of POM. Without the stress of TBBPA, the POM increased the survival rate, reduced the duration of the germination stage, and augmented the plant height. However, under TBBPA stress, the results in Figure 3 (a) and Figure 3 (b) show that the tall wheatgrass not only had later germination, but also had lower survival rates. It was also observed that the soil–POM–TBBPA exhibited slower survival response than the other samples, indicating a significant negative impact on germination in the polluted soil with POM. The results show that the fresh POM in polluted soil increased the negative effects of the TBBPA, thereby further inhibiting germination. In addition, the TBBPA-affected groups showed growth rates as follows: soil–TBBPA > soil-aged–POM–TBBPA > soil–POM–TBBPA. These results demonstrate that POM in polluted soil can also hinder the growth of tall wheatgrass, resulting in

long-term damage to the local ecosystem. Therefore, in contrast to the unpolluted soil–POM condition, which had a higher surface height and survival rate than the pure soil condition, the polluted soil–POM condition showed poorer germination and less growth than the polluted soil without POM, suggesting that POM compounded the toxic effect of TBBPA. Considering that TBBPA has a toxic effect in its own right in terms of inhibiting plant germination and growth [32, 47], the increased effect of the inhibition effects of TBBPA in the presence of POM that was observed in our study may suggest that, during the interaction with the vegetation, the TBBPA adsorbed in the POM was in fact transferred into the tall wheatgrass with the help of the POM (rather than being immobilized on its surface).

Figure 3 (c), Figure 3 (d), and Figure 3 (e) show the resulting indices of each sample at 95 days. Figure 3 (c) shows that the root length, surface length, total height of tall wheatgrass in the presence of POM all decreased after the introduction of TBBPA. However, all samples with POM added had higher total height and longer length than the soil-only samples, indicating that, although the POM with TBBPA could hinder growth at the early stages, under abiotic aging, the POM could ultimately contribute to the survival and viability of tall wheatgrass. Furthermore, aging of the POM resulted in longer root growth compared to contaminated POM, suggesting that the aged POM sustained less negative impact from TBBPA. This is also illustrated by Figure 3 (d) and Figure 3 (e), which show that, under contamination, the aged-POM had higher a survival rate and total weight than unaged POM. Thus, POM under long-term aging could induce less negative effects from pollutants compared to freshly applied POM.

To further characterize the TBBPA transport behaviors between POM and vegetation, particle

samples were acquired from pots of fresh POM, aged POM, and regular soil. Assisted by the second-derived post-treatment (Figure S11 and S12), the detailed distribution of the functional groups on their surface were revealed using an FPA–FTIR spectroscope (Figure S13) . To highlight the alterations of the functional groups on the surface, the invert signal of processed results was applied in Figure 3. Such results not only signify the presence of POM, but also imply that the carboxyl groups on fresh POM may be altered during the growth of the vegetation, as the fresh POM was found to have aromatic structures similar to those of the aged POM. In terms of nutrient utilization by the vegetation, our results indicate that, despite the influence of TBBPA, the vegetation with POM may still have higher utilization of SOM than does the regular soil. This conclusion is supported by the enhanced growth state of the specimens in the presence of POM by the end of the observation.

Thus, though the polluted POM was found to increase the growth of the vegetation without inhibiting the transferal of nutrients, under the influence of POM, the vegetation exhibited vulnerability to the toxic effects of TBBPA, indicating that, when contaminated by organic pollutants, sites with POM may sustain higher damage to local flora. Moreover, although the aged POM had relatively higher adsorption performance than the fresh POM, the impact was observed to be significantly lower than that of fresh contaminated POM, indicating that POM could in the long term reduce the transfer of TBBPA to vegetation. Furthermore, in light of the constant impact of fresh POM after 95 days of observation and the TBBPA-related groups found on their surface as observed in our study, the long-term toxic exposure of the local environment due to the slow release of TBBPA contaminants prior to aging was identified as a significant hazard, especially for regions with a mild climate where frequent freeze-thaw cycles are not

likely to occur.

References

1. Hale, S.; Hanley, K.; Lehmann, J.; Zimmerman, A.; Cornelissen, G., Effects of Chemical, Biological, and Physical Aging As Well As Soil Addition on the Sorption of Pyrene to Activated Carbon and Biochar. *Environmental science & technology* **2011,** *45*, (24), 10445-10453.
2. Xin, X.; Huang, G.; Liu, X.; An, C.; Yao, Y.; Weger, H.; Zhang, P.; Chen, X., Molecular toxicity of triclosan and carbamazepine to green algae Chlorococcum sp.: A single cell view using synchrotron-based Fourier transform infrared spectromicroscopy. *Environmental pollution* **2017,** *226*, 12-20.
3. Lau, K.; Hobro, A.; Smith, T.; Thurston, T.; Lendl, B., Label-free non-destructive in situ biochemical analysis of nematode Steinernema kraussei using FPA-FTIR and Raman spectroscopic imaging. *Vibrational Spectroscopy* **2012,** *60*, 34-42.
4. George, J.; Azad, L. B.; Poulose, A. M.; An, Y.; Sarmah, A. K., Nano-mechanical behaviour of biochar-starch polymer composite: Investigation through advanced dynamic atomic force microscopy. *Composites Part A: Applied Science and Manufacturing* **2019,** *124*, 105486.
5. Richard, S.; Rajadurai, J. S.; Manikandan, V., Influence of particle size and particle loading on mechanical and dielectric properties of biochar particulate-reinforced polymer nanocomposites. *International Journal of Polymer Analysis and Characterization* **2016,** *21*, (6), 462-477.
6. Rahmanian, O.; Dinari, M.; Abdolmaleki, M. K., Carbon quantum dots/layered double hydroxide hybrid for fast and efficient decontamination of Cd(II): The adsorption kinetics and isotherms. *Applied Surface Science* **2018,** *428*, 272-279.
7. Fasfous, I. I.; Radwan, E. S.; Dawoud, J. N., Kinetics, equilibrium and thermodynamics of the sorption of tetrabromobisphenol A on multiwalled carbon nanotubes. *Applied Surface Science* **2010,** *256*, (23), 7246-7252.
8. Yan, B.; Niu, C. H.; Wang, J., Analyses of Levofloxacin Adsorption on Pretreated Barley Straw with Respect to Temperature: Kinetics, π–π Electron-Donor–Acceptor Interaction and Site Energy Distribution. *Environmental science & technology* **2017,** *51*, (14), 8048-8056.
9. Zhang, Y.; Tang, Y.; Li, S.; Yu, S., Sorption and removal of tetrabromobisphenol A from solution by graphene oxide. *Chemical Engineering Journal* **2013,** *222*, 94-100.
10. de Franco, M. A. E.; de Carvalho, C. B.; Bonetto, M. M.; de Pelegrini Soares, R.; Féris, L. A., Diclofenac removal from water by adsorption using activated carbon in batch mode and fixed-bed column: Isotherms, thermodynamic study and breakthrough curves modeling. *Journal of Cleaner Production* **2018,** *181*, 145-154.
11. Wang, P.; Cao, M.; Wang, C.; Ao, Y.; Hou, J.; Qian, J., Kinetics and thermodynamics of adsorption of methylene blue by a magnetic graphene-carbon nanotube composite. *Applied Surface Science* **2014,** *290*, 116-124.
12. Senthilkumaar, S.; Kalaamani, P.; Porkodi, K.; Varadarajan, P. R.; Subburaam, C. V., Adsorption of dissolved Reactive red dye from aqueous phase onto activated carbon prepared from agricultural waste. *Bioresource Technology* **2006,** *97*, (14), 1618-1625.
13. Oke, I. A.; Olarinoye, N. O.; Adewusi, S. R. A., Adsorption kinetics for arsenic removal from aqueous solutions by untreated powdered eggshell. *Adsorption* **2008,** *14*, (1), 73-83.
14. Zhu, J.; Pigna, M.; Cozzolino, V.; Caporale, A. G.; Violante, A., Sorption of arsenite and arsenate on ferrihydrite: Effect of organic and inorganic ligands. *Journal of Hazardous Materials* **2011,** *189*, (1), 564-571.
15. Peak, D.; Ford, R. G.; Sparks, D. L., An in Situ ATR-FTIR Investigation of Sulfate Bonding Mechanisms on Goethite. *Journal of Colloid and Interface Science* **1999,** *218*, (1), 289-299.